Dry Printing Conductive Circuit Traces on Water-Soluble Papers

Adib Taba,[1] Zabihollah Ahmadi,[1] Aarsh Patel,[1] Parvin Fathi-Hafshejani,[1] Seungjong Lee,[2,3] Shuai Shao,[2,3] Michael C. Hamilton,[1,4] Nima Shamsaei,[2,3] Masoud Mahjouri-Samani[1,3,4*]

[1]Electrical and Computer Engineering Department, Auburn University, Auburn, AL 36849, USA.
[2]Department of Mechanical Engineering, Auburn University, Auburn, AL 36849, USA.
[3]National Center for Additive Manufacturing Excellence (NCAME), Auburn University, Auburn, AL 36849, USA.
[4]Alabama Micro/Nano Science and Technology Center (AMNSTC), Auburn University, Auburn, AL 36849, USA.
*Corresponding author: mahjouri@auburn.edu

Abstract

Printed electronics are gaining significant interest due to design flexibility, low fabrication cost, and rapid design-to-manufacturing turnaround. Conventional substrates for printed electronics are often based on non-biodegradable polymers such as polyimide that pose high environmental challenges by creating massive e-waste and pollution. As the demand for printed electronics and sensors increases, the ability to print such devices on biodegradable substrates can provide a solution to such environmental problems. However, current printing technologies are based on liquids/inks that are incompatible with biodegradable substrates, such as paper. Here we present a dry-printing process, namely a dry additive nanomanufacturing (Dry-ANM) technique, for printing conductive silver lines and patterns on biodegradable papers for flexible hybrid papertronics. Pure and dry nanoparticles are generated by pulsed laser ablation of a silver target that are then transported through a nozzle and directed onto paper substrates, where they are deposited and laser-sintered in real-time to form the desired pattern without damaging the paper. The effects of different printing parameters on the paper-burning threshold are investigated, and the electrical properties of the lines are characterized by using different line thicknesses and sintering laser power densities. In addition, the mechanical and electrical properties of the printed lines and patterns are evaluated by bending and twisting tests. Furthermore, the feasibility of printing silver on different paper types is demonstrated. This research can potentially lead to biodegradable and environmentally friendly printed electronics and sensors.

Keywords: Papertronics, printed electronics, additive nanomanufacturing, dry printing, biodegradable electronics

Introduction

The interest in additive manufacturing of functional devices, particularly printed electronics, has been growing with the rise of the Internet of Things (IoT). There has been a demand for printing functional structures and devices for a wide range of applications, including electronics, healthcare, aerospace, and transportation. [1-10] Printing electronics on non-biodegradable plastics and polymers such as polyimide escalating E-waste formation.[11] The use of biodegradable substrates in manufacturing printed electronics can reduce their negative environmental impact.

Paper electronics or papertronics is emerging as an alternative approach for manufacturing electronics and sensors printed on lightweight, flexible, and biocompatible paper substrates when the environment allows. Printing electronics on paper or other biodegradable materials can help recycle and dispose of these devices, as they can be broken down more easily than traditional non-biodegradable substrates. Excellent features of cellulose paper, including biodegradability, biocompatibility, strength, and lightweight, make it a unique potential substrate for electronics. [12-14]

Due to the potential environmental advantages of paper substrates, researchers have attempted printing various devices on paper substrates, [15, 16] such as temperature sensors, [17] humidity sensors, [17] electrochemical sensors, [18-21] biosensors, [22-24] antennas, [25] composite life monitoring sensors [26] and wearable devices. [22, 27] Various methods have been used to print electronics on paper substrates, including inkjet printing (IJP) and aerosol jet printing (AJP). [28-33] For instance, Huang et al. [34, 35] printed silver nanoparticles using IJP on a photo paper substrate that has a polymer coating. For this purpose, they prepared the polyacrylic acid-coated silver nanoparticle ink for a process of more than 24 hours. The printed silver was reported to reach a resistivity of 1.26×10^{-7} Ω·m at room temperature and 4.7×10^{-8} Ω·m after sintering at 150 °C. However, it was observed that the photo paper would degrade after 60 ° C. Patil et al. [36] printed silver using nanowire inks on regular printing paper and found that the high concentration (50 $mg \cdot mL^{-1}$) of the ink leads to a resistivity as low as 4.3×10^{-5} Ω·m. Landers et al. [37] penetrated wax into the paper to make it compatible with liquid inks.

The current printing technologies are liquid/ink-based methods incompatible with biodegradable substrates, especially paper. Due to the porous nature of fibrous paper, the liquid inks wet the paper, and the liquid penetrates deeper into the substrate due to the capillary effect. Controlling the capillary effect and avoiding the deformation of the paper due to the wet process make the printing operation extremely challenging and often impossible. On the other hand, using coated substrates like photo paper or waxed papers to avoid wetting increases the required processing and decreases the biodegradability of the paper. Apart from issues of the ink specifically for printing on paper, other ink-associated issues include the impurity and high cost of ink production. [38-40]

To overcome the aforementioned challenges, this study utilized a dry additive nanomanufacturing (Dry-ANM) method to print conductive silver patterns on biodegradable paper for future papertronics. The ANM method was recently developed and demonstrated for inkless printing of clean materials on rigid and flexible substrates. [41-43] In the current application of this technique, pure silver nanoparticles were created by pulsed laser ablation of a solid silver target. These nanoparticles were then guided via a carrier gas out of the printer nozzle and onto the substrates, where they were deposited and laser-sintered in real-time to form the desired patterns without damaging the paper. The paper burning threshold was investigated under various printing parameters, and the electrical characteristics of the lines were characterized for different conductor thicknesses and laser power densities. Furthermore, the electrical stability of the printed lines due to mechanical conditions was studied by bending and twisting tests. These results, for the first time, show the possibility of direct printing conductive lines on untreated biodegradable papers.

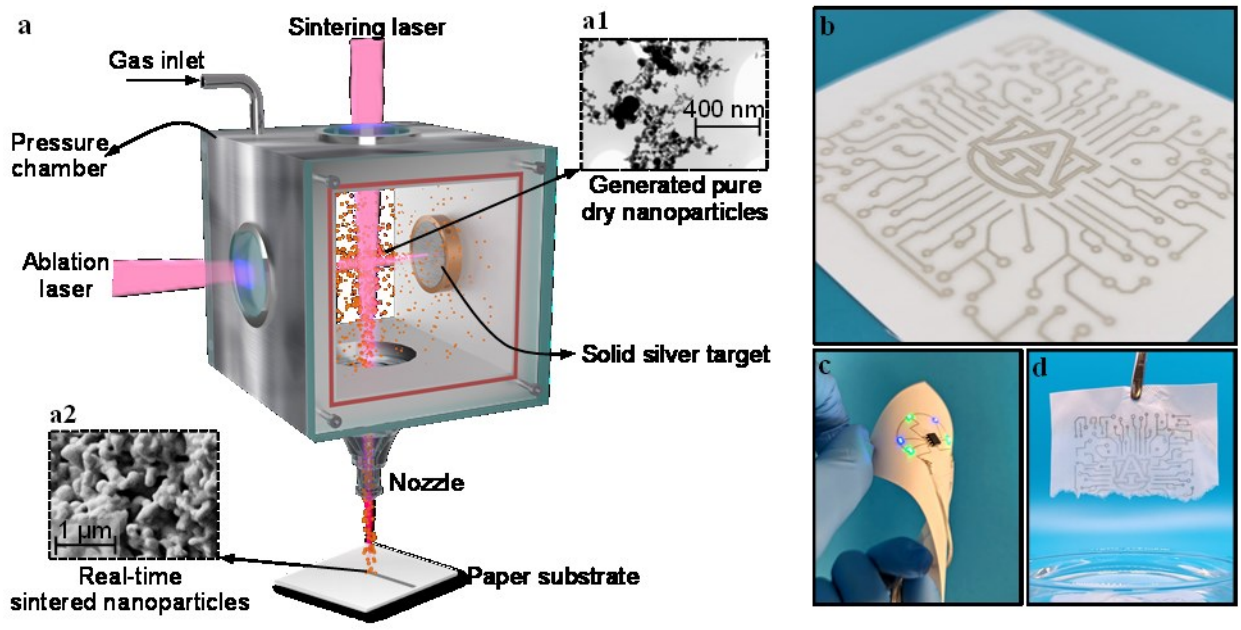

Figure 1. (**a**) Schematic illustration of the Dry-ANM system used for printing silver traces on paper substrates. Subfigures are STEM (a1) and SEM (a2) images of generated and sintered nanoparticles, respectively. (**b**) An example of a conductive silver pattern on a biodegradable paper. Demonstrations of (**c**) A printed blinking LED circuit on the paper showing the successful performance (see **Movie S1** in Supporting Information) and (**d**) fast (20 s) water solubility (see **Movie S2** in Supporting Information). The Auburn University logo is used with permission.

Experimental Section

A schematic view of the apparatus for the Dry-ANM system is shown in **Figure 1a**. The apparatus includes an ablation laser (1064 nm pulsed nanosecond laser), a mini chamber, a solid silver target, a sintering laser (1064 nm pulsed nanosecond laser), a nozzle, an X-Y positioning stage, and a controlled gas inlet. The ablation laser beam coupled to a galvo scanner was directed into the chamber and focused onto the silver target's surface to generate nanoparticles. The laser interaction with the silver target causes the materials to be ablated. The interaction of these ablated species with the background argon gas results in condensation and the formation of nanoparticles. A scanning transmission electron microscopy (STEM) image presents an example of generated nanoparticles, as shown in **Figure a1**. For printing and sintering the nanoparticles into desired patterns, argon gas flow transports a stream of nanoparticles toward the nozzle. The nozzle creates a jet flow from the tip of the nozzle to the surface of the paper substrates. The momentum of the nanoparticles during the jet flow causes them to collide with the surface of the paper, and at the same time, the sintering laser beam is directed onto the substrate's surface, where the nanoparticles land. The controlled interaction of the sintering laser with the nanoparticles leads to the localized heating and sintering of nanoparticles without burning the paper. An example of sintered nanoparticles on paper is presented by scanning electron microscopy (SEM) image in **Figure a2**. The programmable movement of the X-Y stage creates the desired pattern during this process. The Dry-ANM technique enables the printing of silver patterns (**Figure 1b**) and circuits (**Figure 1c**) on biodegradable substrates that are also fast water-soluble (**Figure 1d**), or fast disposable.

The quality of printed lines can be controlled by process parameters such as ablation laser power, chamber pressure, nozzle diameter, sintering laser power density, X-Y stage (printing) speed, and the number of printed layers. The selected parameters for all experiments in this study are stated in the Methods and Characterizations section or otherwise mentioned in the text.

Results and Discussions

Nanoparticle Generation and Characterization

To investigate the laser-generated silver nanoparticle size distribution, the nanoparticles were deposited on paper and also on TEM grids without any laser sintering process. The SEM and STEM images of unsintered silver nanoparticles on the paper and the TEM grids are shown in **Figures 2a-d**. By analyzing the images using ImageJ (Supporting Information **Figure S1**), the size distribution of the nanoparticles was estimated to be in the range of 3 to 120 nm. More details are provided on the size distribution histogram and its log-normal distribution curve fit (**Figure 2e**), where the mean and median of particle diameter are 18.5 nm and 15.4 nm, respectively. The small nanoparticle size makes the particles' sintering feasible at lower temperatures compared to microparticles and can potentially lead to higher-resolution lines and printed features.

The same STEM images have been taken for different chamber pressure and ablation laser power density. Our qualitative observation indicated that changing chamber pressure from 5 to 20 psig did not significantly affect the size of the nanoparticles (Supporting Information **Figure S2**). However, increasing the ablation laser power density increased the nanoparticles' size (Supporting Information **Figure S3**).

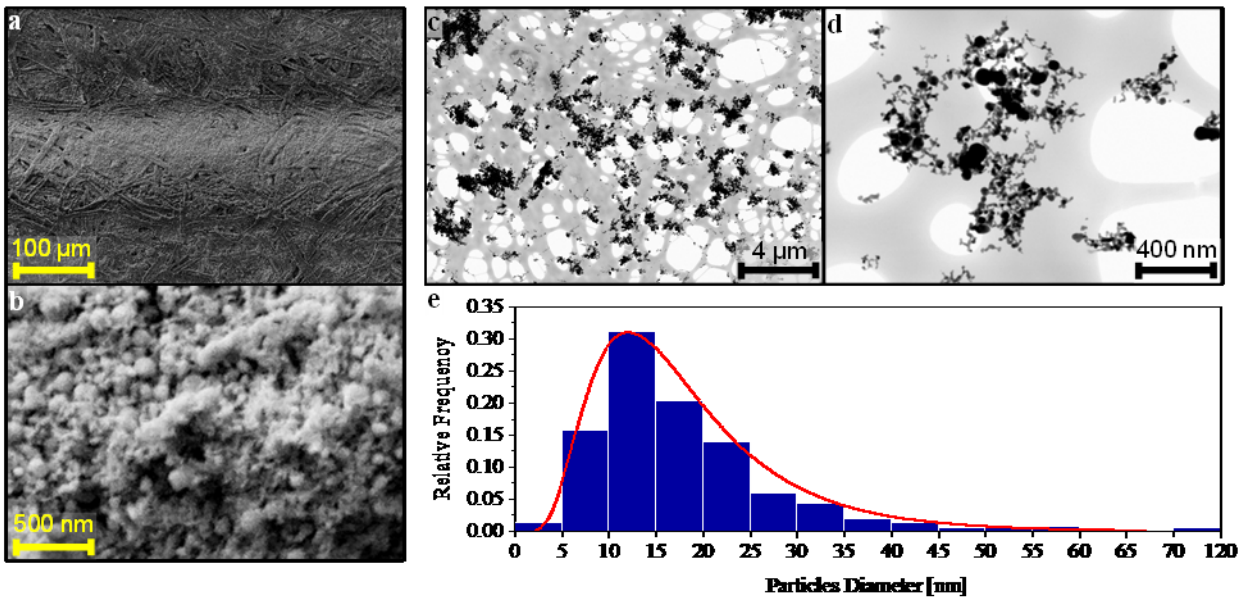

Figure 2. (**a, b**) SEM images of the unsintered silver nanoparticles on paper. (**c, d**) STEM image of unsintered silver nanoparticles on TEM grid. (**e**) Nanoparticles' size distribution histogram and log-normal distribution curve fit (grey line) were derived from analyzing the STEM images.

Paper-Burning Threshold in Relation to Sintering Laser Process Parameters

Systematic experiments were performed to understand the effects of different process parameters on the paper substrates and to specifically determine survivability and burning thresholds. The

paper burning was quantified visually from no burning level (level 0) to a completely burnt level (level 5) (**Figure 3a**). The results of the burning threshold of paper with the presence of nanoparticles and sintering laser for different printing speeds and sintering laser power densities are shown in **Figure 3b**. The printing time for all printing speeds was kept constant at 100 seconds by increasing the number of printed layers at higher speeds. This ensured the sintering of nominally the same amount of nanoparticles on each printed line. The results showed that high printing speeds (16 and 14 mm/s) prevented the temperature rise on the surface of the paper while laser sintering the nanoparticles. Fast passing over lines helped with more uniform energy distribution to the line in a short period, just enough to sinter the nanoparticles but insufficient to conduct heat to the paper and burn it. Also, the wide range of safe process windows (levels 1 to 3) at these speeds demonstrated that rapidly passing over small burned spots avoids further extension of these spots. For the same concept, decreasing the speed to 6 mm/s decreased the burning threshold (i.e., the paper started to burn at lower power densities) due to the sufficient heat transfer and temperature rise for burning to take place. Also, it should be noted that the absorption of these white papers at the sintering laser wavelength (1064 nm) was relatively low. However, as soon as its color became darker due to the unwanted temperature rise, the absorption increased and burning accelerated drastically.

Reducing the speed to lower values, such as 0.2 mm/s, increased the energy density and temperature over a small spot area. However, after nanoparticles were sintered, the energy absorption of the surface decreased, and most of the laser energy was not absorbed on the surface, creating a safe self-limiting sintering process. Furthermore, the number of printed layers was decreased for lower speeds, i.e., 2 layers for 0.2 mm/s compared to 20 layers for 2 mm/s. However, a minor surface abnormality (e.g., dark spots) could lead to high absorption and complete burning of the line. The effect of the number of printed layers on the burning threshold is presented in **Figure 3c** for a speed of 12 mm/s. These results verified the delayed burning at low pass counts and how the repetition over the same line could advance a burning spot. **Figures 3d-e** display the SEM images of a small burning spot (the onset of burning, level 1), and **Figures 3f-g** display the burning development at level 4.

We further performed the above experiments without the presence of nanoparticles (i.e., no ablation) or gas and just using a sintering laser. The paper did not burn on selected power densities under these conditions. It is due to the low absorbance of these white papers under the sintering laser wavelength (i.e., 1064 nm) used in our experiments. Pagès et al. [44] demonstrated that the paper absorbs less than 2% irradiated light in the wavelength range of 800 nm to 1300 nm. This selective laser sintering would be beneficial for the Dry-ANM method to avoid paper burning and only increase the temperature of the silver nanoparticles sufficient for sintering.

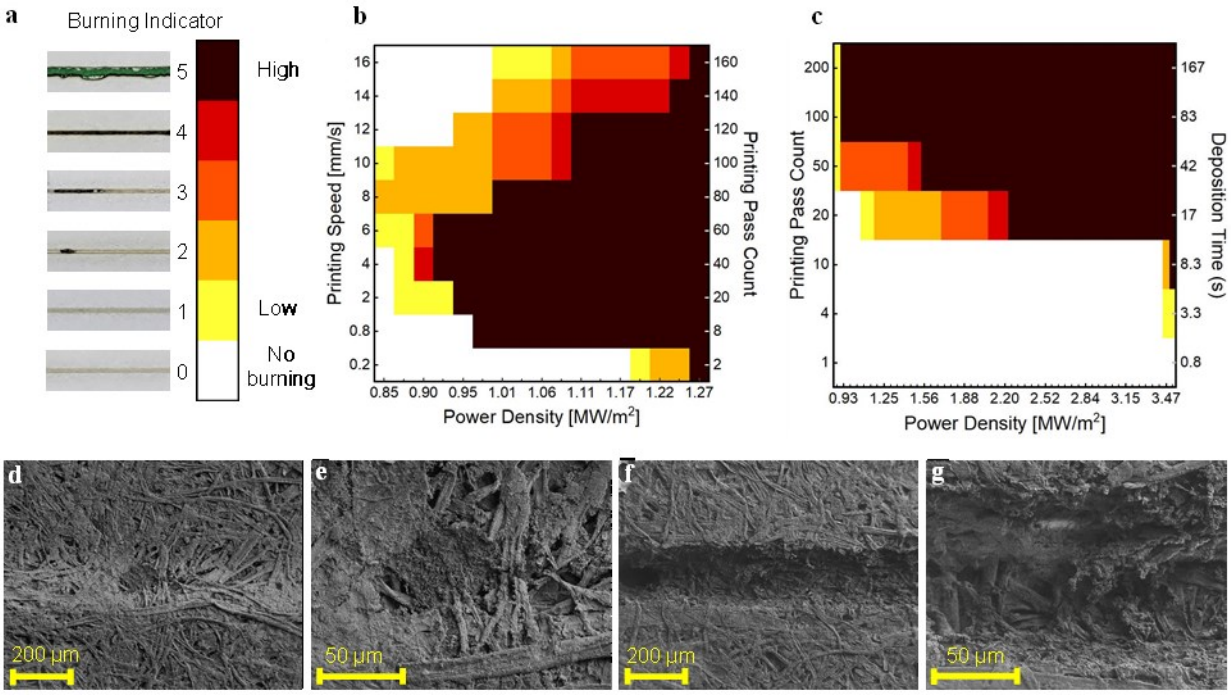

Figure 3. (**a**) Optical images of 1-cm silver lines printed on paper. The burning indicator corresponds to each level of burning, with 0 showing no burning and 5 indicating complete burning of the line. Burning threshold of paper with the presence of particles and sintering laser for (**b**) printing speed versus the sintering laser power density (at constant deposition time of 100 s), and (**c**) the number of printed layers versus the sintering laser power density (at a constant printing speed of 12 mm/s). SEM images of the printed silver lines on paper starting from (**d-e**) the onset of burning (Level 1) to (**f-g**) deep burning (Level 4).

Electrical Properties and Topology of the Printed Silver Lines

After understanding the burning threshold of the paper substrates, the effects of power density and printing pass count on the electrical properties and topography of the printed silver lines were studied. A set of lines were printed and sintered for various printing pass counts and power densities below the paper burning threshold. The thickness of the lines was measured using optical profilometry, and resistance was measured using the 4-probe measurement method. **Figures 4a-b** show the optical images of a selection of printed lines from this study, and **Figures 4c** represents the typical topography of a sintered silver line. The profilometer results showed a thickness of ~11 µm (Supporting Information **Figure S4**) for power densities below 0.7 MW/m^2 (**Figure 4e**). The thickness was slightly reduced at higher power density (still below the burning threshold) due to better sintering of and formation of denser silver films. The resistance was also decreased after increasing the power density to more than 0.2 MW/m^2 (**Figure 4f**). As shown in **Figure 4g**, the resistivity of the silver lines continuously decreased with the increase of the sintering laser power density. On inspection of the optical images shown in **Figure 4g**, we see that better sintering at higher power densities changes the color of the line from black to silver. It should be noted that the unsintered printed nanoparticles have a dark appearance, and sufficient laser sintering changes their color to silver. A similar study was conducted for different printing pass counts at a fixed power density. Increasing the number of printed passes increased the thickness of the lines linearly (**Figure 4h**). The resistance results (**Figure 4i**) showed a sharp decrease as the number of passes

increased, and the resistivity (**Figure 4j**) followed the same trend. The typical sintered silver line width was measured to be about ~300 µm using a 260-micron nozzle (**Figure 4d**). While it is a reasonable value for the 260 µm nozzle used in this work, improving the resolution would be an important future scope for increasing the utility of this Dry-ANM approach.

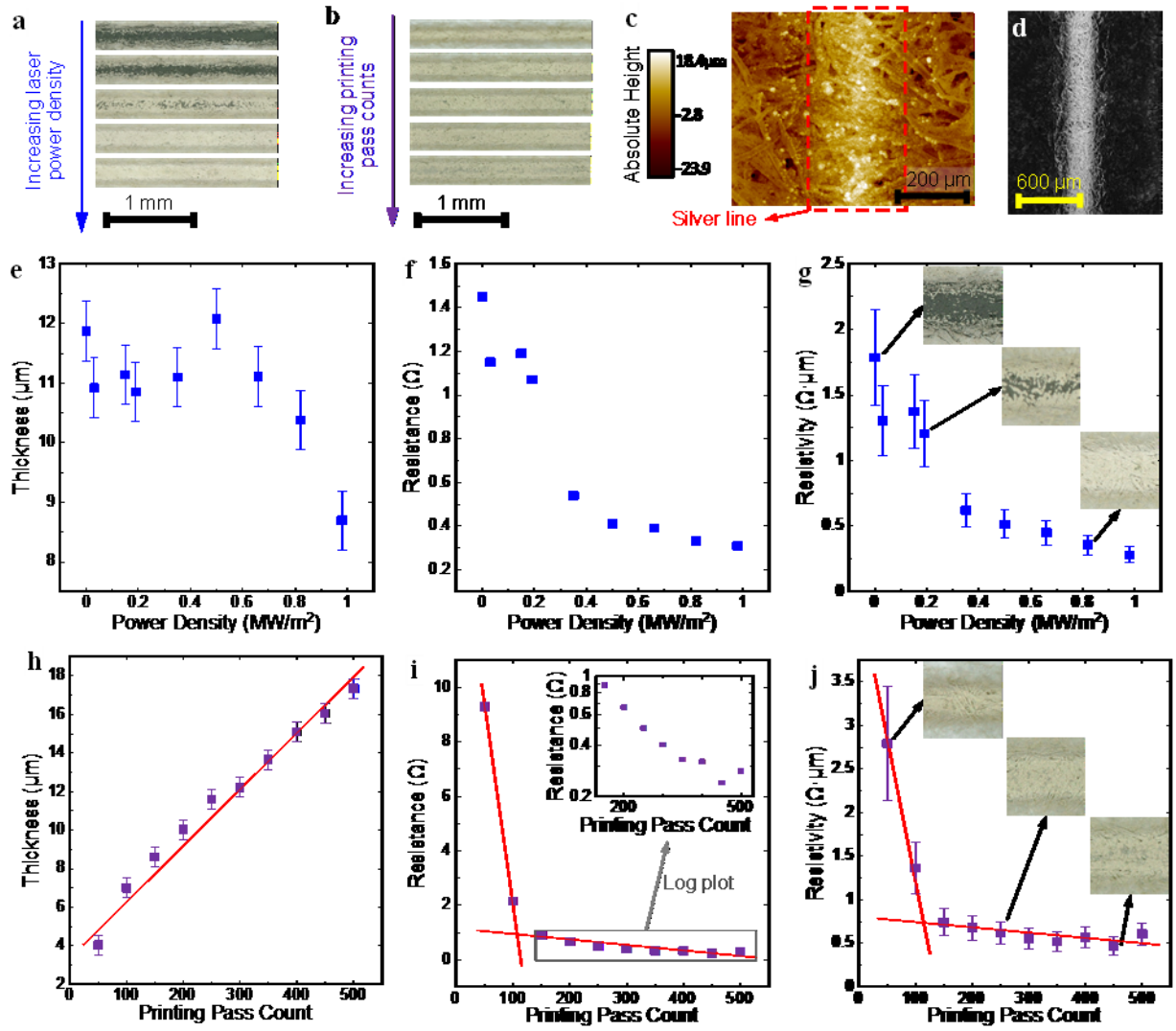

Figure 4. Optical images of the printed silver lines for various (**a**) power densities and (**b**) printing pass counts. (**c**) A 3D profilometry image of a sintered silver line. (**d**) A BSE image of the silver line to show better contrast between the silver and substrate. (**e**) Thickness, (**f**) resistance, and (**g**) resistivity graphs for various sintering laser power densities. (**h**) Thickness (the red line is the linear fit of the data), (**i**) resistance (the inset is the log plot of the boxed section), and (**j**) resistivity graphs as a function of printing pass count (i.e., number of printed layers). Error bars indicate the measurement uncertainty of one trial. For details about error bars, see supporting information **Section S4**.

Figure 5 shows the SEM images of the printed lines prepared in the above power density study. The thickness of the lines where the sintering laser was off (power density = 0 MW/m^2), looked

more than other sintered images due to the fluffiness of the unsintered deposition. Higher sintering power densities of 0.01, 0.19, and 0.82 MW/m^2 clearly showed a transition from small unsintered nanoparticles to partially sintered nanoparticles and, finally, a completely sintered network of connected structures. These results were consistent with the thickness and resistance graphs (**Figure 4e-j**). By increasing the power density, the sintered nanoparticles created a solid skeletal network that increased the conductivity, and at the same time, the densification caused the thickness to decrease.

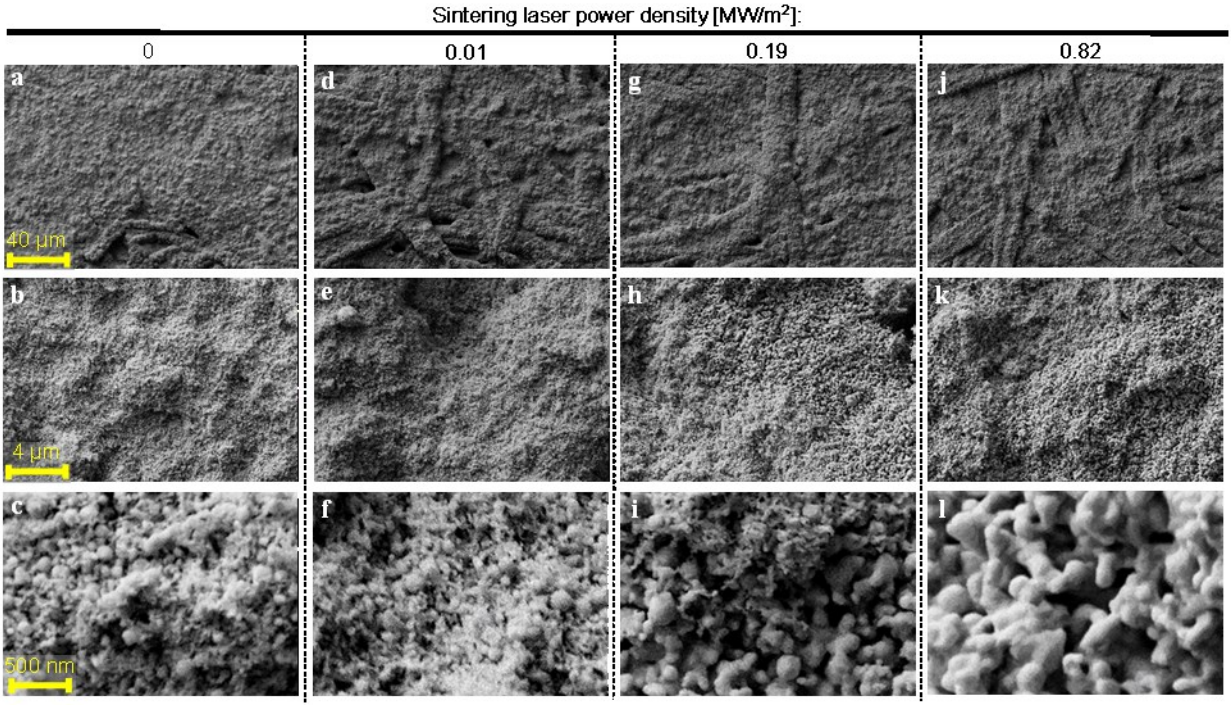

Figure 5. SEM images of printed lines for various sintering laser power densities. (**a-c**) No sintering, magnification, (**d-f**) 0.01 [MW/m^2], (**g-i**) 0.19 [MW/m^2], (**j-l**) 0.82 [MW/m^2]. The scale bar of images in the same row is equal. Higher power densities clearly show a transition from small unsintered nanoparticles to a fully sintered network of connected structures.

We further performed a printing pass study, as shown by the SEM images in **Figure 6**. As soon as the thickness of the sintered silver nanoparticles advanced above the fibers' height in the paper, the resistance decreased drastically (**Figure 4i**). As the thickness further increased, the resistance decreased with a slower slope and finally plateaued. As shown in **Figure 6**, no significant changes were observed in the morphology of the printed/sintered lines as the pass count increased.

We further examined the impact of extra laser sintering on the printed silver lines without the deposition of new nanoparticles for different sintering passes (0, 4, 8, and 12), and different sintering laser power densities (See Supporting Information for detail). We observed the formation of a slightly more solid network by further laser sintering the printed lines. For example, the resistivity further dropped close to 1.9×10^{-7} Ω·m by 8 extra laser sintering passes with a power density of 0.93 MW/m^2.

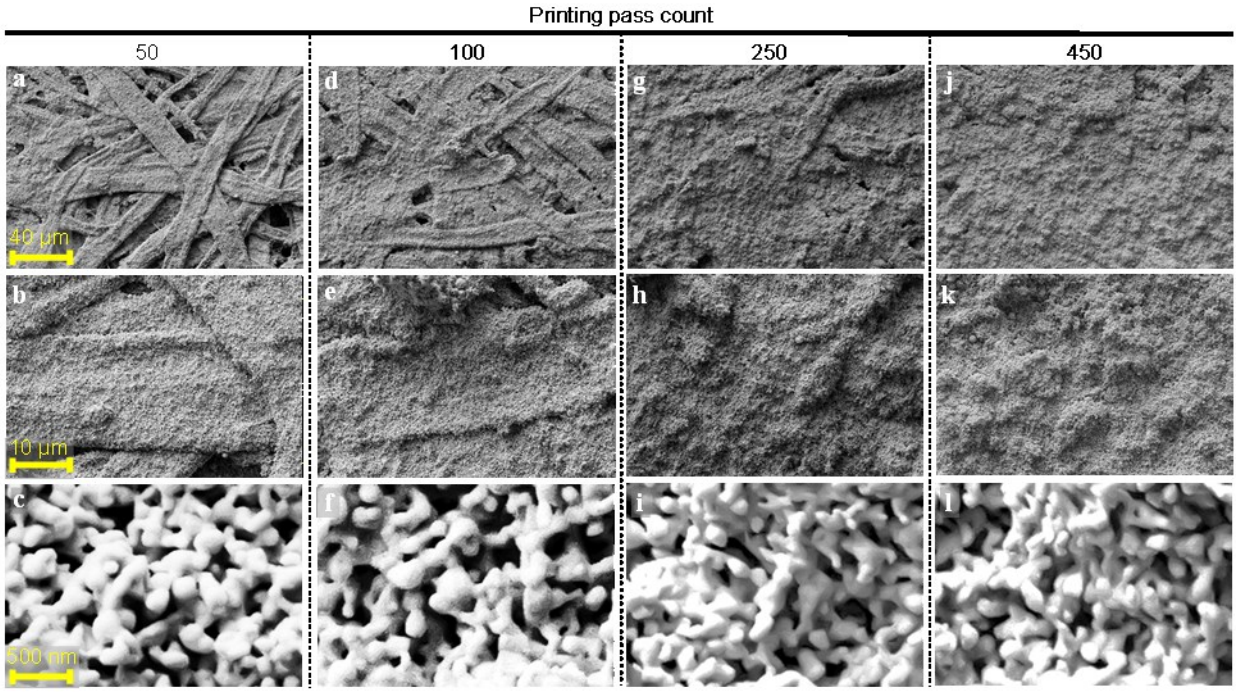

Figure 6. SEM images of the printed lines for various printing pass counts (i.e., number of layers). (**a, c**) 50, (**d-f**) 100, (**g-i**) 250, (**j-l**) 450 pass counts. No significant changes were observed in the morphology of the sintered line as the pass count increased. The scale bar of images in the same row is equal.

Detailed interfacial analysis between the printed silver traces and the paper substrate was performed using focused ion beam-scanning electron microscopy (FIB-SEM). Cross-sectional imaging was carried out by milling the sample with a gallium ion beam. The high-resolution image was obtained using a BSE detector (**Figures 7a-e**). These images enabled direct visualization of the print morphology with the underlying paper topography and underscored the lack of localized burning beneath the silver lines. Higher magnification imaging on the silver part displayed the skeletal nanostructure resulting from sintering the printed silver nanoparticles, verifying successful fusion into a conductive network (**Figure 7b**). By analyzing **Figure 7b** using ImageJ, the porosity of the sintered silver was estimated to be %49.5. **Figures 7a**, along with its zoom-in images (**Figure 7c-e**) demonstrated that the printed silver traces resided predominantly on the paper surface, with the silver nanoparticles generally not penetrating deep into the paper pores. Occasional infiltration into surface pores up to one fiber layer deep (**Figures 7c-e**) made sure of the adhesion of silver to the paper. However, the majority of the printed trace remained on the top of the paper fibers. Energy dispersive X-ray spectroscopy (EDS) elemental mapping (**Figures 7f-g**) and spectrum (**Figure 7h**) over the region shown in **Figure 7d** verified the presence of metallic silver on the paper surface rather than absorbed into the pores (**Figures 7f-h**). More EDS mapping and spectrum are presented in Supporting Information **Figures S7-S8**. The EDS mapping and spectrum from a cross-section of an as-received clean paper substrate is included in Supporting Information **Figures S9**.

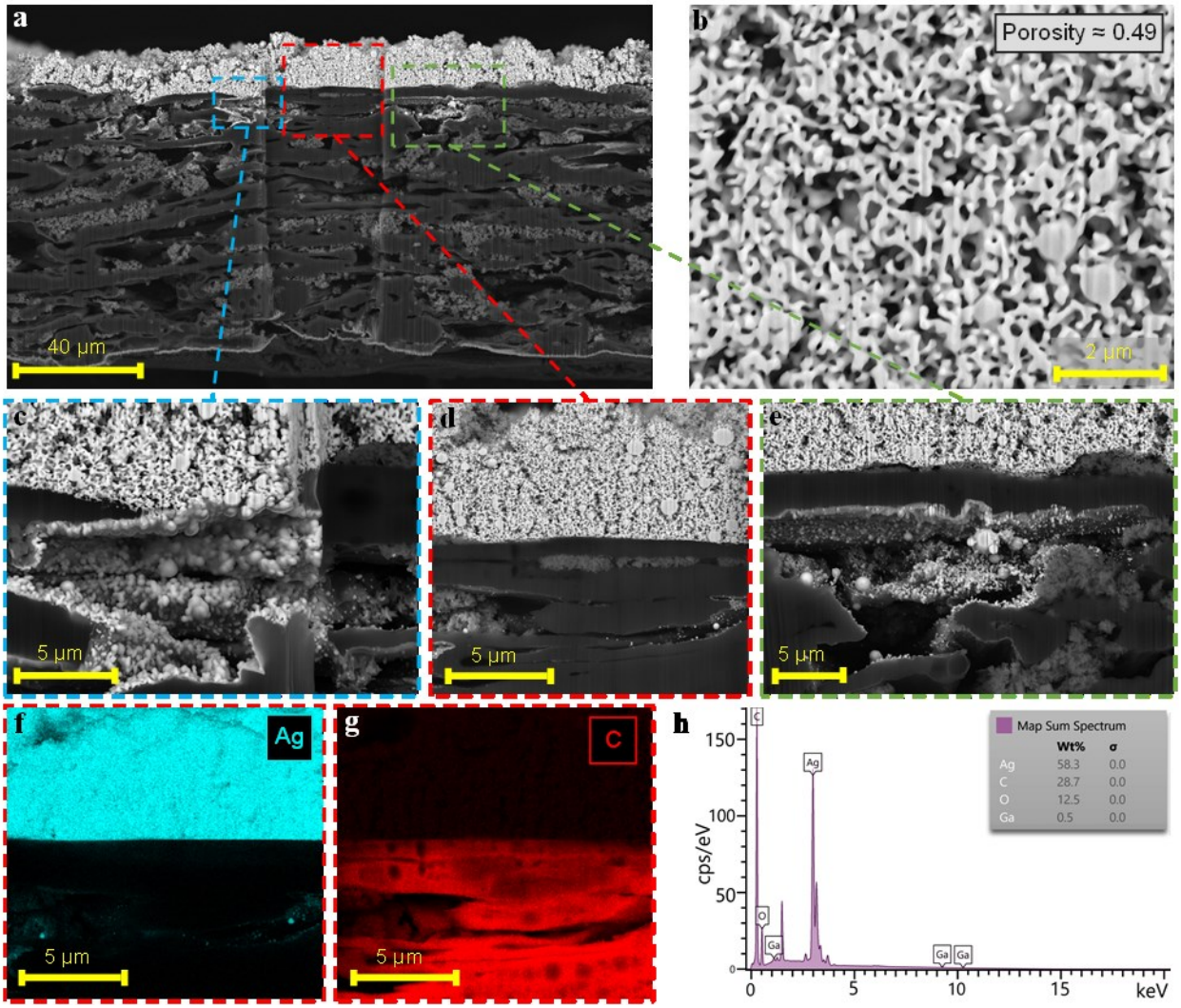

Figure 7. (**a**) Cross-sectional BSE image of a printed silver trace on a paper substrate prepared by a FIB-SEM. (**b**) Higher magnification BSE image of the cross-section showing sintered nanoparticle network. (**c**) BSE image zoomed on pore (visible from the top) with silver infiltration. (**d**) BSE image showing silver atop the paper surface. (**e**) BSE image zoomed on a pore with limited silver infiltration showing silver not filling the pore channels. EDS map showing the (**f**) silver and (**g**) carbon distributions. (**h**) EDS spectrum of detected elements.

Reliability Tests

The flexibility and reliability of the printed lines were evaluated by static and cyclic bending and twisting tests. **Figures 8a-b** shows the custom-made bending and twisting machines used in this experiment (see **Movie S3** in the Supporting Information). These tests were performed on 12 mm×0.2mm silver lines (thickness 10 µm) printed on paper under various bending radii and twisting angles at three different cycles (1, 10, and 100k). The percentage of resistance change from the initial value before the test and the final value after the test was measured. The results for the bending tests are shown in **Figures 8c-e**. No resistance change was observed for a bending radius of more than 17 mm, and it slightly changed for bending radii of 15 mm and 13.5 mm. A test circuit with programmed flashing LEDs was also printed to demonstrate its functionality under

bending stress. To attach the LEDs, a silver paste was applied and allowed to dry at room temperature for 1 hour. As shown in **Figure 8f**, the circuit performed its function under various bending conditions (see **Movie S1** in Supporting Information). For twisting experiments, pieces of 12mm×5mm paper with printed silver lines on the longitudinal direction were prepared and tested. The resistance change results of the samples due to torsion stress are shown in **Figures 8g-i**. The initial resistance change happened at twisting angles of 130°, 90°, and 90° for 1k, 10k, and 100k cycles, respectively. An example of the twisting capability of silver lines on a LED circuit is shown in **Figure 8j**. In addition to conducting bending and twisting tests, it is important to investigate other environmental factors, such as temperature and humidity tests, to ensure the functionality and time-dependent durability of the dissolvable paper circuits.

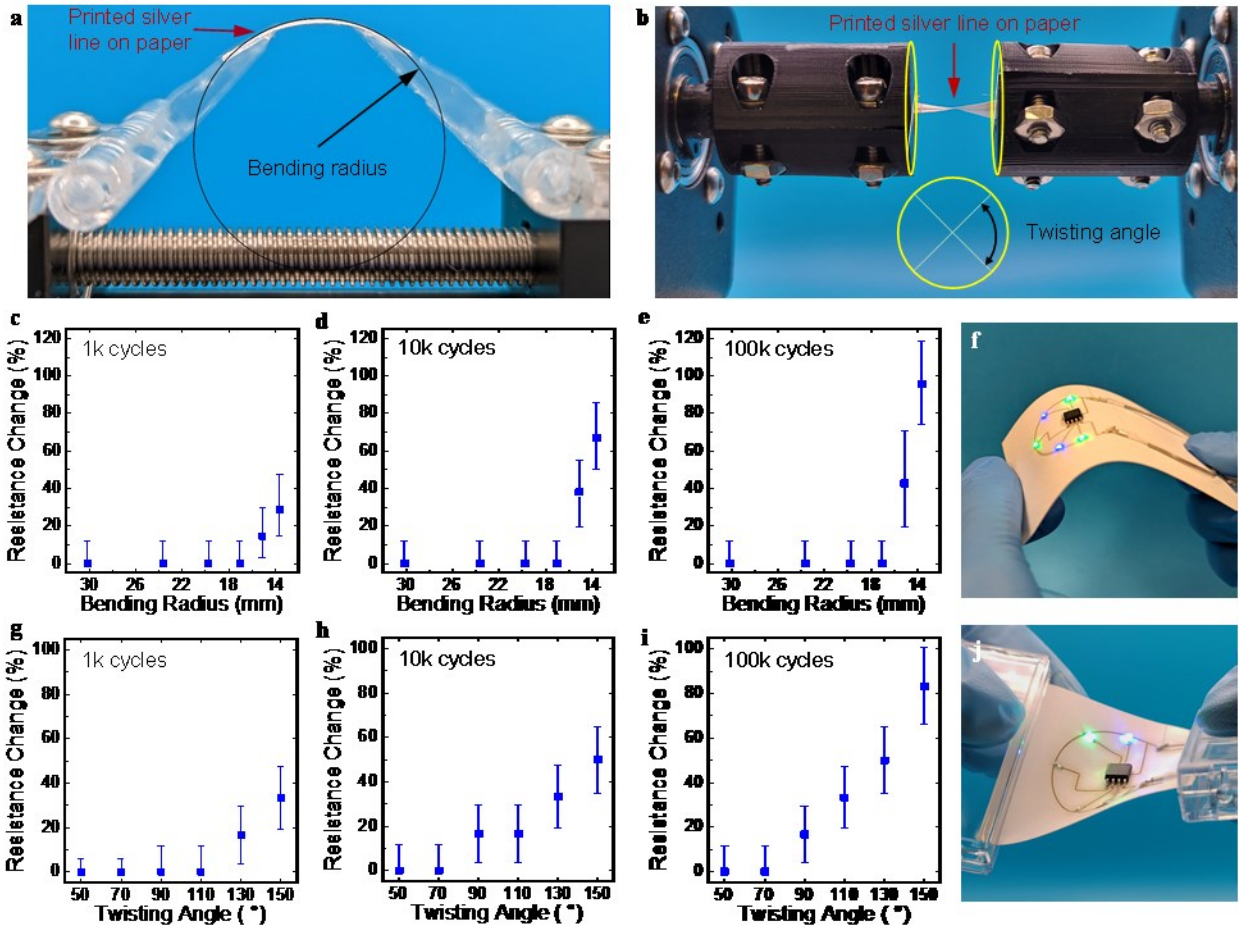

Figure 8. Digital photos of custom-made (**a**) bending and (**b**) twisting apparatus. The percentage of resistance change under (**c**) 1k, (**d**) 10k, and (**e**) 100k bending cycles. Bending strains correspond to bending radius data points ranging from 30 mm to 14 mm are 21.1, 16.6, 13.8, 11.9, 10.6, and 9.5, respectively. (**f**) A printed blinking LED circuit showing successful performance under various bending conditions. The percentage of resistance change under (**g**) 1k, (**h**) 10k, and (**i**) 100k twisting cycles. Torsional strains correspond to twisting angle data points ranging from 50° to 150° are 87, 122, 157, 192, 227, and 262, respectively. (**j**) Performance example of a twisted blinking LED circuit. Error bars indicate the measurement uncertainty of three trials. For details about error bars, see supporting information **Section S4**.

Printing Patterns on Different Papers: Testing Water Solubility

Figure 9a shows the ability to print on different papers with various densities, including 32 lb (90 gsm) printing paper, 24 lb (120 gsm) printing paper, cleanroom paper, and fast water-soluble paper. The process parameters were optimized based on each of the substrates. The printing outcomes were successful on all of these papers without damaging or burning them. We did not observe significant variations in the electrical resistance of the printed lines on different papers. To test the water solubility of the printed patterns, samples printed on fast water-soluble papers were submerged in water, and their degradation was observed. The printed silver lines, including micro and nanoparticles, remained in the water. Silver could be considered to irrigate plants since studies have shown the advantages of silver nanoparticles for enhancing plant growth and crop productivity.[45] The silver particles could even be recycled by using separation techniques like electrophoresis.[46] Digital images of a dissolving sample in 17 seconds are presented in **Figure 9b** (see **Movie S2** in Supporting Information). While the water-solubility of paper-based printed electronics can address the future e-waste problem, besides their use as transient electronics for security and military applications, further work is needed to recover and recycle the silver and electronic components.

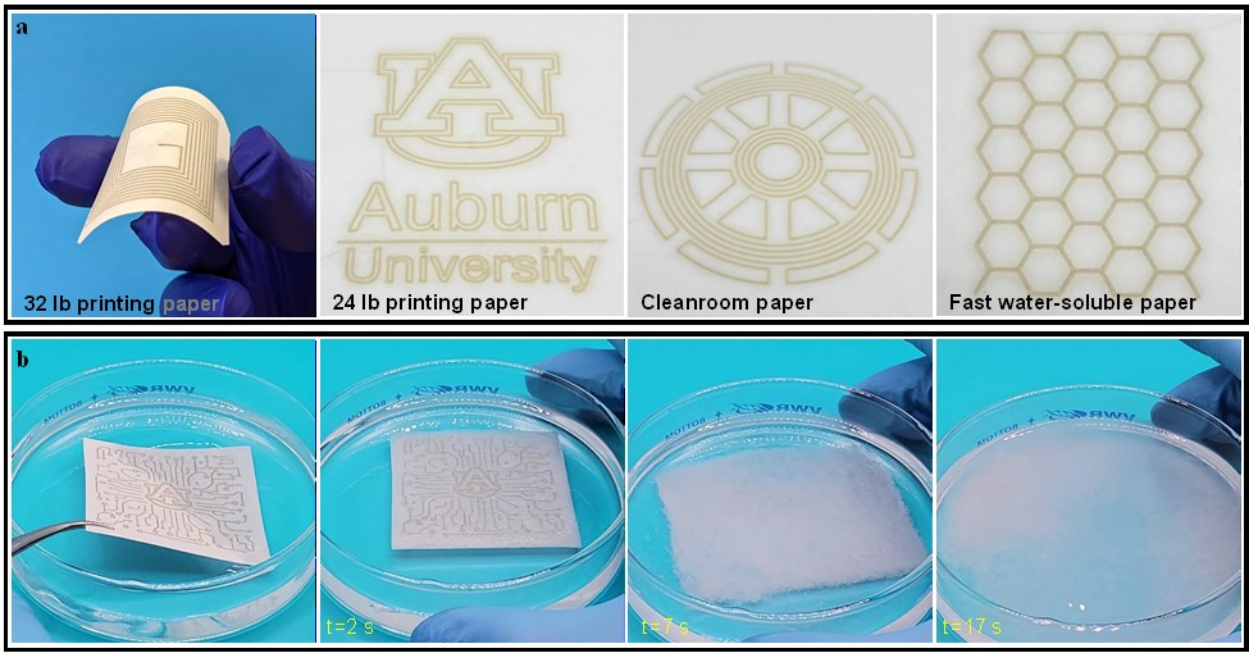

Figure 9. (**a**) Printed conductive silver patterns on various types of papers. From left to right: 32 lb printing paper, 24 lb printing paper, cleanroom paper, and fast water-soluble paper. Demonstrating the (**b**) fast water-solubility. The Auburn University logo is used with permission.

Conclusion

In summary, dry printing of pure silver traces on paper as a biodegradable substrate was demonstrated using an ANM method. In this method, dry nanoparticles from a solid target were generated using a pulsed laser ablation technique. The nanoparticles were transferred to the surface of the paper substrate through a nozzle using argon as a carrier gas. At the same time, another laser sinters the nanoparticles on the paper below its burning threshold while achieving good electrical conductivity of the formed silver film. The generated nanoparticle size distribution was in the range of 3 to 120 nm with an average of 18.5 nm. The burning threshold of the paper for various

sintering laser power densities and printing layers was evaluated. The electrical properties and topography of the printed silver lines were investigated using optical profilometry, electrical resistance, SEM, and optical images. Resistivity measurements with values as low as 2×10^{-7} Ω·m were achieved. In addition, static and cyclic bending and torsion tests demonstrated the printed lines' excellent mechanical and electrical properties. No change was observed in printed lines' mechanical and electrical properties for a 17 mm bending radius and 70° twisting angle through 100k bending and torsion cycles. These results, along with demonstrations of fast water solubility and considering extensions of this work to other dry printable materials (including dielectric materials) are highly promising for future biodegradable flexible electronics with applications in a wide range of fields, including electronics, healthcare, aerospace, and transportation.

Methods and Characterizations

The solid target, substrate, and inert gas used in experiments are silver (99.99% pure, 1 in diameter from Kurt J Lesker), regular printing paper (24 lb and 32 lb Hammermill Premium laser print copy paper), and argon, respectively. The 5pt fast water-soluble paper was purchased from SmartSolve.

For in situ dry nanoparticles generation, the power of the ablation laser, ablation laser frequency, ablation laser hatching speed, and chamber pressure were set to 22 W, 20 kHz, 500 mm/s, and 5 psig, respectively. A 1064 nm pulsed nanosecond laser with 1mj/puls was used for the ablation and the sintering laser had the same specification.

For printing and sintering purposes, the sintering laser power density, nozzle diameter, nozzle-substrate gap, X-Y stage (printing) speed, and printing pass count were set to 0.66 MW/m^2, 260 µm, 1.5 mm, 12 mm/s, 200, respectively.

SEM, BSE, and EDS images were taken using a Zeiss Crossbeam 550 FIB-SEM equipped with BSD4 and EDS detectors. The same microscope in transmission mode with a STEM detector was used to obtain STEM images from TEM sample grids.

To prepare the paper cross-section, a sharp cutter was used to cut the paper. Then the deformed area due to the cutter was cut out using high-current ion beam milling (30 kV, 30 nA). After that, fine milling was applied with low-current ion beam milling (30 kV, 7 nA). The Zeiss Crossbeam 550 FIB-SEM was used for gallium ion beam milling.

A KEYENCE VHX-6000 series microscope was used for optical images of the printed silver lines.

For calculating the resistivity, resistance was measured with a 4-probe measurement method using a Keithley 2400 SourceMeter.

The thickness and height profiles of the samples were measured using an optical profilometer (MicroXAM-800 optical profiler, KLA Tencor). The total scan area for each sample was 600µm × 750µm, and a 1µm z-axis step size was used.

Acknowledgments

This material is based upon work partially supported by the U.S. National Science Foundation (NSF) under grants No. 2134024 and No. 2018794. Alabama Micro/Nano Science and Technology Center (AMNSTC) at Auburn University provided access to the electrical measurement facility. National Center for Additive Manufacturing Excellence (NCAME) at Auburn University provided access to imaging facilities.

Conflict of Interest

The authors declare no conflict of interest.

Author Contributions

A.T. designed and performed the experimental setup, synthesis and processing experiments, materials characterization, data analysis, and manuscript writing. Z.A participated in the synthesis, processing and printing experiments. A.P. performed the reliability tests and performance analysis. A. T., and P.F. participated in the electric characterization, reliability tests and data analysis. A. T., and S.L. participated in sample cross-sectional preparation. S.L. participated in SEM, STEM, BSE, and EDS imaging and data analysis. S.S., M.C.H., and N.S. participated in design of experiments, data analysis, and discussions. M.M.S. led the project, participated in experimental design, data acquisition and analysis, discussions, and manuscript preparation. All of the authors participated in manuscript preparation and revision processes.

Supporting Information

Supporting information is available online: Post processing images using ImageJ; STEM images of silver nanoparticles for various chamber pressure and ablation laser power densities; Profilometry images and the approach to calculate the average thickness; Explanation of error bars and uncertainty calculations; SEM images of printed lines for various resintering pass count and laser power density without particle deposition after printing; EDS maps details from the cross-section of a paper with printed silver and as-received clean paper substrate; Calculation of bending strain and torsional strain; and List of supplementary movies showing the flexibility capability of a paper LED circuit, water solubility of a printed demo circuit, and custom-made bending machines.

References

1. Shah, M.A., et al., *Classifications and appLications of inkjet printing technology: A review.* IEEE Access, 2021. **9**: p. 140079-140102.
2. Park, Y.G., et al., *High-Resolution 3D Printing for Electronics.* Adv Sci (Weinh), 2022. **9**(8): p. e2104623.
3. Shrivas, K., et al., *Inkjet-printed paper-based colorimetric sensor coupled with smartphone for determination of mercury (Hg2+).* Journal of Hazardous Materials, 2021. **414**: p. 125440.
4. Yang, P., et al., *Printed Zinc Paper Batteries.* Adv Sci (Weinh), 2022. **9**(2): p. e2103894.
5. Li, Z., et al., *Inkjet Printed Disposable High-Rate On-Paper Microsupercapacitors.* Advanced Functional Materials, 2022. **32**(1): p. 2108773.
6. Pan, T., et al., *A flexible, multifunctional, optoelectronic anticounterfeiting device from high-performance organic light-emitting paper.* Light Sci Appl, 2022. **11**(1): p. 59.
7. Aeby, X., et al., *Fully 3D Printed and Disposable Paper Supercapacitors.* Adv Mater, 2021. **33**(26): p. e2101328.
8. Li, M., et al., *A highly integrated sensing paper for wearable electrochemical sweat analysis.* Biosens Bioelectron, 2021. **174**: p. 112828.
9. Enfield, R.E., et al., *The future of 3D food printing: Opportunities for space applications.* Crit Rev Food Sci Nutr, 2022: p. 1-14.
10. Fathi-Hafshejani, P., et al., *Two-Dimensional-Material-Based Field-Effect Transistor Biosensor for Detecting COVID-19 Virus (SARS-CoV-2).* ACS Nano, 2021. **15**(7): p. 11461-11469.

11. Irimia-Vladu, M., et al., *Green and biodegradable electronics.* Materials Today, 2012. **15**(7-8): p. 340-346.
12. Seddiqi, H., et al., *Cellulose and its derivatives: towards biomedical applications.* Cellulose, 2021. **28**(4): p. 1893-1931.
13. Cao, Y. and K.E. Uhrich, *Biodegradable and biocompatible polymers for electronic applications: A review.* Journal of Bioactive and Compatible Polymers, 2019. **34**(1): p. 3-15.
14. Brunetti, F., et al., *Printed Solar Cells and Energy Storage Devices on Paper Substrates.* Advanced Functional Materials, 2019. **29**(21): p. 1806798.
15. Soum, V., et al., *Programmable Paper-Based Microfluidic Devices for Biomarker Detections.* Micromachines (Basel), 2019. **10**(8): p. 516.
16. Wiklund, J., et al., *A Review on Printed Electronics: Fabrication Methods, Inks, Substrates, Applications and Environmental Impacts.* Journal of Manufacturing and Materials Processing, 2021. **5**(3): p. 89.
17. Lall, P., K. Goyal, and J. Narangaparambil. *Accuracy, Hysteresis and Extended Time Stability of Additively Printed Temperature and Humidity Sensors*. in *2020 IEEE 70th Electronic Components and Technology Conference (ECTC)*. 2020. IEEE.
18. Deroco, P.B., D. Wachholz, and L.T. Kubota, *Silver Inkjet-Printed Electrode on Paper for Electrochemical Sensing of Paraquat.* Chemosensors, 2021. **9**(4): p. 61.
19. Beduk, T., et al., *A paper-based inkjet-printed PEDOT:PSS/ZnO sol-gel hydrazine sensor.* Sensors and Actuators B-Chemical, 2020. **306**: p. 127539.
20. Wustoni, S., et al., *Enzyme-Free Detection of Glucose with a Hybrid Conductive Gel Electrode.* Advanced Materials Interfaces, 2019. **6**(1): p. 1800928.
21. Smith, S., et al., *Printed Paper-Based Electrochemical Sensors for Low-Cost Point-of-Need Applications.* Electrocatalysis, 2019. **10**(4): p. 342-351.
22. Maier, D., et al., *Toward Continuous Monitoring of Breath Biochemistry: A Paper-Based Wearable Sensor for Real-Time Hydrogen Peroxide Measurement in Simulated Breath.* ACS Sens, 2019. **4**(11): p. 2945-2951.
23. Bihar, E., et al., *A fully inkjet-printed disposable glucose sensor on paper.* Npj Flexible Electronics, 2018. **2**(1): p. 30.
24. Li, X., et al., *Enhancing the performance of paper-based electrochemical impedance spectroscopy nanobiosensors: An experimental approach.* Biosens Bioelectron, 2021. **177**: p. 112672.
25. Chakraborty, M., F. Nikbakhtnasrabadi, and R. Dahiya, *Hybrid integration of screen-printed RFID tags and rigid microchip on paper.* IEEE Journal on Flexible Electronics, 2022. **1**(2): p. 107-113.
26. Siddique, S., et al., *M3D aerosol jet printed buckypaper multifunctional sensors for composite structural health monitoring.* Results in Physics, 2019. **13**: p. 102094.
27. Gao, Y., M. Rezaie, and S. Choi, *A Wearable, Disposable Paper-based Self-Charging Power System Integrating Sweat-driven Microbial Energy Harvesting and Energy Storage Devices.* Nano Energy, 2022: p. 107923.
28. Pan, Y.Y., et al., *Optical Printing of Conductive Silver on Ultrasmooth Nanocellulose Paper for Flexible Electronics.* Advanced Engineering Materials, 2022. **24**(7): p. 2101598.
29. Wang, L. and J. Liu, *Ink Spraying Based Liquid Metal Printed Electronics for Directly Making Smart Home Appliances.* Ecs Journal of Solid State Science and Technology, 2015. **4**(4): p. P3057-P3062.

30. Siegel, A.C., et al., *Foldable Printed Circuit Boards on Paper Substrates.* Advanced Functional Materials, 2010. **20**(1): p. 28-35.
31. Dagdeviren, C., et al., *Conformal piezoelectric energy harvesting and storage from motions of the heart, lung, and diaphragm.* Proceedings of the National Academy of Sciences of the United States of America, 2014. **111**(5): p. 1927-1932.
32. Liu, Z.H., et al., *Flexible Indium-Tin-Oxide Homojunction Thin-Film Transistors with Two In-Plane Gates on Cellulose-Nanofiber-Soaked Papers.* Advanced Electronic Materials, 2019. **5**(7): p. 1900235.
33. Lamas-Ardisana, P.J., et al., *Disposable electrochemical paper-based devices fully fabricated by screen-printing technique.* Electrochemistry Communications, 2017. **75**: p. 25-28.
34. Huang, Q.J., et al., *Properties of polyacrylic acid-coated silver nanoparticle ink for inkjet printing conductive tracks on paper with high conductivity.* Materials Chemistry and Physics, 2014. **147**(3): p. 550-556.
35. Shen, W., et al., *Preparation of solid silver nanoparticles for inkjet printed flexible electronics with high conductivity.* Nanoscale, 2014. **6**(3): p. 1622-8.
36. Patil, P., et al., *Inkjet printing of silver nanowires on flexible surfaces and methodologies to improve the conductivity and stability of the printed patterns.* Nanoscale Adv, 2021. **3**(1): p. 240-248.
37. Landers, M., et al., *Integrated Papertronic Techniques: Highly Customizable Resistor, Supercapacitor, and Transistor Circuitry on a Single Sheet of Paper.* ACS Appl Mater Interfaces, 2022. **14**(40): p. 45658-45668.
38. Uzun, S., et al., *Additive-free aqueous MXene inks for thermal inkjet printing on textiles.* Small, 2021. **17**(1): p. 2006376.
39. Cui, Y., et al., *Over 16% efficiency organic photovoltaic cells enabled by a chlorinated acceptor with increased open-circuit voltages.* Nat Commun, 2019. **10**(1): p. 2515.
40. Lemarchand, J., et al., *Challenges, Prospects, and Emerging Applications of Inkjet-Printed Electronics: A Chemist's Point of View.* Angew Chem Int Ed Engl, 2022. **61**(20): p. e202200166.
41. Ahmadi, Z., et al., *Dry Printing and Additive Nanomanufacturing of Flexible Hybrid Electronics and Sensors.* Advanced Materials Interfaces, 2022. **9**(12): p. 2102569.
42. Ahmadi, Z., et al., *Additive Nanomanufacturing of Multifunctional Materials and Patterned Structures: A Novel Laser-Based Dry Printing Process.* Advanced Materials Technologies, 2021. **6**(5): p. 2001260.
43. Ahmadi, Z., et al., *Inkless Multimaterial Printing Flexible Electronics by Directed Laser Deposition at Nano-and Microscale.* ACS Applied Nano Materials, 2023.
44. Pages, H., et al., *Demonstration of paper cutting using single emitter laser diode and infrared-absorbing ink.* Opt Express, 2005. **13**(7): p. 2351-7.
45. Khan, S., et al., *The impact of silver nanoparticles on the growth of plants: The agriculture applications.* Heliyon, 2023. **9**(6): p. e16928.
46. Hwang, J.S., et al., *Recycling silver nanoparticle debris from laser ablation of silver nanowire in liquid media toward minimum material waste.* Sci Rep, 2021. **11**(1): p. 2262.

Table of Contents.

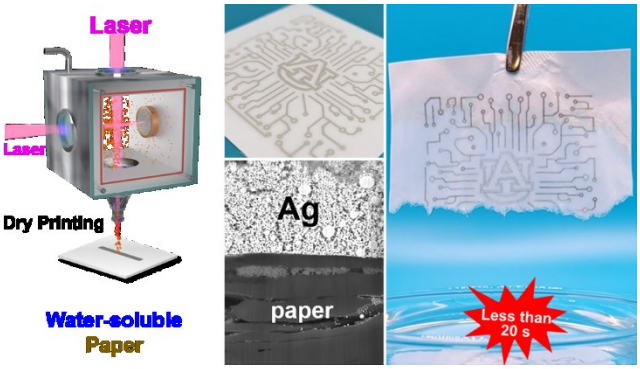

Synopsis: Dry printing of conductive silver on paper enables sustainable electronics through water dissolution. The Auburn University logo is used with permission.